remote sensing

MDPI

Article

Forward-Looking Super-Resolution Imaging of MIMO Radar via Sparse and Double Low-Rank Constraints

Junkui Tang, Zheng Liu *, Lei Ran, Rong Xie and Jikai Qin

National Laboratory of Radar Signal Processing, Xidian University, Xi'an 710071, China
* Correspondence: lz@xidian.edu.cn

Abstract: Multiple-input multiple-output (MIMO) radar uses waveform diversity technology to form a virtual aperture to improve the azimuth resolution of forward-looking imaging. However, the super-resolution imaging capability of MIMO radar is limited, and the resolution can only be doubled compared with the real aperture. In the radar forward-looking image, compared with the whole imaging scene, the target only occupies a small part. This sparsity of the target distribution provides the feasibility of applying the compressed sensing (CS) method to MIMO radar to further improve the forward-looking imaging resolution. At the same time, the forward-looking imaging method for a MIMO radar based on CS has the ability to perform single snapshot imaging, which avoids the problem of a motion supplement. However, the strong noise in the radar echo poses a challenge to the imaging method based on CS. Inspired by the low-rank properties of the received radar echoes and the generated images, and considering the existing information about sparse target distribution, a forward-looking super-resolution imaging model of a MIMO radar that combines sparse and double low-rank constraints is established to overcome strong noise and achieve robust forward-looking super-resolution imaging. In order to solve the multiple optimization problem, a forward-looking image reconstruction method based on the augmented Lagrangian multiplier (ALM) is proposed within the framework of the alternating direction multiplier method (ADMM). Finally, the results of the simulation and the measurement data show that the proposed method is quite effective at improving the azimuth resolution and robustness of forward-looking radar imaging compared with other existing methods.

Keywords: multiple-input multiple-output (MIMO); forward-looking imaging; compressed sensing (CS); sparse and double low-rank constraints; augmented Lagrangian multiplier (ALM); alternating direction multiplier method (ADMM)

check for updates

Citation: Tang, J.; Liu, Z.; Ran, L.; Xie, R.; Qin, J. Forward-Looking Super-Resolution Imaging of MIMO Radar via Sparse and Double Low-Rank Constraints. *Remote Sens.* **2023**, *15*, 609. https://doi.org/10.3390/rs15030609

Academic Editor: Andrea Monti Guarnieri

Received: 1 December 2022
Revised: 8 January 2023
Accepted: 18 January 2023
Published: 19 January 2023

Copyright: © 2023 by the authors. Licensee MDPI, Basel, Switzerland. This article is an open access article distributed under the terms and conditions of the Creative Commons Attribution (CC BY) license (https://creativecommons.org/licenses/by/4.0/).

1. Introduction

Forward-looking imaging is critical in some civil and military applications, such as precision guidance, the autonomous landing of aircraft, terrain mapping [1–4], etc. However, due to the limitations of the imaging mechanisms, traditional monostatic imaging methods, including synthetic aperture radar (SAR) and Doppler beam sharpening (DBS), cannot achieve forward-looking high-resolution imaging [5,6]. At present, a forward-looking image is mainly obtained by the real beam imaging method, and its azimuth resolution is limited by the size of the antenna, which is insufficient for practical applications [7,8]. Therefore, how to break through the restriction of the real beam resolution and achieve forward-looking super-resolution imaging has important application value.

Multiple-input multiple-output (MIMO) radar combines waveform diversity and array technology to form observation channels that are far greater in number than the actual number of physical antennas. The multiple observation channels conduct echo data acquisition in a parallel manner in space, thus enabling MIMO radar to have potential real-time imaging capabilities without compensating for the motion of the platform [9–11]. By combining the coherent processing of the multichannel echo data, MIMO radar can

achieve a higher spatial resolution than a real aperture array [12]. Generally, the virtual array formed by MIMO radar is twice as large as the actual aperture, while the traditional imaging methods of MIMO radar, such as back projection (BP) [13,14] and range migration (RM) [15,16], do not have the ability of super-resolution. In order to further improve the forward-looking imaging resolution, it is necessary to combine MIMO radar with the super-resolution imaging method.

In recent years, the compressed sensing (CS) theory has been widely used in radar imaging [17–19]. The CS theory shows that the accurate recovery of high-dimensional sparse signals can be achieved by obtaining a small amount of data by observation [20]. In forward-looking imaging, compared to the entire imaging scene, the target we focus on occupies a small part, so we consider that the target is distributed sparsely in the scene, which is why the application of the CS method to MIMO radar to improve forward-looking imaging resolution provides feasibility. Moreover, the CS-based MIMO radar imaging method has been demonstrated to have the capability of real-time imaging, which can avoid the problems of motion compensation and large amounts of data [21–24]. Therefore, many CS-based MIMO radar imaging methods have been proposed. In [25], Hu et al. proposed a method for reconstructing high-quality target images using CS when the MIMO radar transmit waveforms are not orthogonal, and the proposed method has strong robustness in noisy environments. In [26], Mitchell et al. proposed a method for obtaining the CS optimal observation matrix by adaptively changing the MIMO radar transmit waveform interval, which has the potential to significantly improve the image restoration effect. In [27], Gu et al. proposed a sparse array single snapshot imaging method for MIMO radar, which not only avoids the motion compensation processing required for traditional SAR imaging but also greatly reduces the number of antenna elements. In [28], Ding et al. reconstructed the measurement matrix of the traditional CS imaging MIMO radar method with the help of the orthogonal matching pursuit (OMP) algorithm, which suppressed the appearance of false targets in the imaging pattern, thereby reducing the reconstruction error. The single snapshot imaging method of the MIMO radar combined with CS has many advantages. However, the strong noise in the radar echo is unavoidable, and the strong noise will destroy the sparsity of the target distribution, resulting in the failure to reconstruct some targets in the generated image or a large number of false targets, which poses a challenge to the CS imaging methods that only utilize the sparse prior information of targets.

In order to enhance the performance of the CS-based imaging method, Qiu et al. [29] presented a joint low-rank and sparse prior (JLRS) ISAR imaging method. The low-rank property of the echo signal and the sparsity of the target are utilized to improve the ISAR imaging performance when data are lost randomly, but the noise is not constrained in the imaging model. Subsequently, Lv et al. [30] proposed a sparse ISAR imaging model that jointly uses sparsity and low rank (JUSLR), and, although the noise is constrained in this model, the constraint capability is limited, and the target region's noise is not effectively suppressed. Zhang et al. [31] found that combining a nonlocal total variation (NLTV) constraint with local sparsity can overcome strong noise and eliminate some spurious strong scattering targets or clutter in ISAR imaging while simultaneously preserving the form and geometry of the target regions. Furthermore, Zeng et al. [32], inspired by the low rank and sparsity of the two-dimensional distribution of the target, presented a novel ISAR reconstruction method. The experimental results demonstrate that this approach provides superior image quality and noise resistance. However, the reconstruction performance is not optimal due to the use of the zero norm of the two-dimensional matrix as the sparsity constraint. Zhang et al. [33] proposed a weighted CS (WCS) method for ISAR image generation, which improved the robustness of the traditional CS algorithm through different weight constraints on the target and noise.

The above research shows that mining more prior information can improve the performance of traditional CS-based imaging methods. Inspired by this, we build a forward-looking imaging model for MIMO radar by combining sparse and double low-rank (CSDLR) priors. Our CSDLR model not only takes into account the fact that targets are sparse in the

forward-looking region but also exploits the fact that the signal matrix in the echoes and the resulting images have low-rank properties. Specifically, the low-rank constraint of the signal matrix in the echo is used to remove noise, and the sparsity of the target distribution and the low-rank characteristics of the image are used to eliminate false or unreliable strong scattering point targets. Moreover, with regard to the resulting multiple optimization issue, the multiplier alternating direction method (ADMM) [34] can effectively solve the constrained optimization problem and converge mildly. The ADMM has been utilized effectively in multiple joint optimizations of ISAR or SAR imaging [35–37]. Therefore, under the ADMM framework, this paper proposes an augmented Lagrange multiplier (ALM) method for efficiently solving our proposed optimization problem model.

This paper is structured as follows: Section 2 presents the forward-looking imaging model of MIMO radar and the CS-based forward-looking super-resolution imaging method. In Section 3, a MIMO radar forward-looking imaging method that combines low rank and sparsity is proposed in detail. In Section 4, the experimental results are presented to demonstrate the effectiveness of our proposed method, and, in Section 5, a conclusion is given.

2. Signal Model

As shown in Figure 1, M transmitting antennas and N receiving antennas are distributed on the same linear array MIMO radar with equal intervals Nd and d, respectively. In order to simplify the subsequent derivation, we place the imaging target and the transceiver antenna on the same plane and consider a two-dimensional imaging scene. At the same time, the coordinate system is established with the center of the imaging scene as the polar coordinate origin. Then, the m-th transmitting antenna and the n-th receiving antenna can be expressed as (R_{T_m}, ϕ_{T_m}) and (R_{R_n}, ϕ_{R_n}), respectively. Suppose that there is a point target $P(x, y)$ in the forward-looking imaging scene, its scattering coefficient is σ, and the distance from the center of the scene is $|r_P|$. Let the distances from the m-th transmitting antenna and the n-th receiving antenna to the point target P be $R^P_{T_m}$ and $R^P_{R_n}$, respectively, and the distance from the center of the array antenna to the center of the scene is R_0. Assume that the m-th transmitted signal is

$$s_{T_m}(t) = u_m(t)e^{j(2\pi f_m t + \varphi_m)} \tag{1}$$

where $u_m(t)$ is the complex envelope of the m-th transmitted signal; for $\forall\tau$, there is $\int u_m(t)u^*_{m'}(t-\tau)dt = 0$ when $m \neq m'$ is satisfied; and f_m and φ_m are the carrier frequency and initial phase of the transmitted signal, respectively. The echo received by the n-th receiving antenna after the reflection of the M transmitted signals through the scattering point P is:

$$b_{R_n}(t) = \sum_{m=1}^{M} \sigma \cdot s_m(t - \tau_{n,m}(x, y)) \tag{2}$$

where $\tau_{n,m}(x, y)$ is the distance time delay from the signal sent from the m-th transmitting antenna, reflected by scattering point P, to the corresponding reception of the n-th receiving antenna. Here, $\tau_{n,m}(x, y)$ can be expressed as

$$\tau_{n,m}(x, y) = \frac{R^P_{T_m}(x, y) + R^P_{R_n}(x, y)}{c} \tag{3}$$

where c is the speed of light. According to the original field hypothesis, we know that if $|r_P| \ll R_{T_m}$ and $|r_P| \ll R_{R_n}$, then

$$R^P_{T_m} \approx R_{T_m} + I_{T_m} \cdot r_P, \quad R^P_{R_n} \approx R_{R_n} + I_{R_n} \cdot r_P \tag{4}$$

where I_{T_m} and I_{R_n} are the unit position vectors from the m-th transmitting antenna and the n-th receiving antenna to the center of the imaging scene, respectively, and they can be expressed as

$$I_{T_m} = (\sin\phi_{T_m}, \cos\phi_{T_m}), \quad I_{R_n} = (\sin\phi_{R_n}, \cos\phi_{R_n}) \tag{5}$$

Then, the time delay $\tau_{n,m}(x,y)$ can be approximately

$$\begin{aligned} \tau_{n,m}(x,y) &\approx \frac{R_{T_m} + I_{T_m} \cdot r_P + R_{R_n} + I_{R_n} \cdot r_P}{c} \\ &= \frac{R_{T_m} + R_{R_n} + x(\sin\phi_{T_m} + \sin\phi_{R_n})}{c} \\ &\quad + \frac{y(\cos\phi_{T_m} + \cos\phi_{R_n})}{c} \end{aligned} \tag{6}$$

The echo $b_{R_n}(t)$ received by the n-th receiving antenna, after the carrier frequency removal, uses the orthogonality of the signal to achieve channel separation, and the output of channel (n,m) is

$$\begin{aligned} b_{n,m}(t) &= \sigma \cdot p_{T_m}(t - \tau_{n,m}) \cdot \exp(-j2\pi f_m \tau_{n,m}) \\ &= \sigma \cdot p_{T_m}(t - \tau_{n,m}) \cdot \exp\left(-j2\pi f_m \frac{R_{T_m} + R_{R_n}}{c}\right) \\ &\cdot \exp\left(-j2\pi f_m \frac{x(\sin\phi_{T_m} + \sin\phi_{R_n})}{c}\right) \\ &\cdot \exp\left(-j2\pi f_m \frac{y(\cos\phi_{T_m} + \cos\phi_{R_n})}{c}\right) \end{aligned} \tag{7}$$

where p_{T_m} is the autocorrelation function of $s_{T_m}(t)$. If the small angle approximation is satisfied in the centralized MIMO radar's configuration, then there are $\cos\phi_{T_m} + \cos\phi_{R_n} \approx 2$, $\sin\phi_{T_m} + \sin\phi_{R_n} \approx \phi_{T_m} + \phi_{R_n}$, and $R_{T_m} + R_{R_n} \approx 2R_0$. If the bandwidth of the transmitted waveform is smaller than the center f_c of the transmitted waveform, then it is $f_m \approx f_c$. Therefore, (7) can be approximated as follows:

$$\begin{aligned} b_{n,m}(t) &\approx \sigma \cdot p_{T_m}(t - \tau_{n,m}) \cdot \exp\left(\frac{-j4\pi f_c R_0}{c}\right) \\ &\cdot \exp\left(\frac{-j4\pi f_c y}{c}\right) \exp\left(-j2\pi f_c \frac{x(\phi_{T_m} + \phi_{R_n})}{c}\right) \end{aligned} \tag{8}$$

where $\exp\left(\frac{-j4\pi f_c R_0}{c}\right)$ is a constant term that can be ignored in (8). Assuming that there are K_0 strong scattering points in the range bin y, and considering the noise e, the echo signal of this bin can be expressed as

$$y = \sum_{k=1}^{K_0} \sigma_k \cdot \exp\left[-j2\pi f_c \frac{x_k(\phi_{T_m} + \phi_{R_n})}{c}\right] + e \tag{9}$$

Since the transmitting antenna and receiving antenna are equally spaced, the following can be obtained from the equivalent phase center:

$$\phi_{T_m} + \phi_{R_n} = 2\phi_s \tag{10}$$

where $\phi_s = (s-1)\Delta\theta_s$, $s = (n-1)M + m$, $s = 1, 2, \ldots, S$, and $S = M \times N$. Here, $\Delta\theta_s$ is the angle interval between the two adjacent antennas of the equivalent transceiver array. From the equivalent array, the azimuth resolution of the forward-looking imaging of the MIMO radar is $\Delta x = \frac{\lambda_c}{2MN\Delta\theta_s}$, where $\lambda_c = c/f_c$. If the abscissa of the scattering point

k is $x_k = q_k \Delta x$, where q_k is a positive integer, then the received echo signal (9) can be expressed as

$$y = \sum_{k=1}^{K_0} \sigma_k \cdot \exp\left[-j2\pi \frac{q_k(s-1)}{S}\right] + e \tag{11}$$

Assuming that the imaging scene contains Q range bins, in the CS-based super-resolution imaging the two-dimensional echo matrix Y can be represented as follows

$$Y = FZ + E = Y_0 + E \tag{12}$$

where $F \in C^{MN \times U}$ is the azimuth dictionary matrix, $U \geq M \times N$. Here, $Y_0 \in C^{MN \times Q}$ is the signal matrix, and $Z \in C^{U \times Q}$and $E \in C^{MN \times Q}$ are the image matrix and noise matrix, respectively. It can be seen from (12) that F is an overcomplete Fourier matrix. When only the prior information of the sparse target distribution is considered, the image matrix Z can be reconstructed by solving the following optimization problems:

$$\min_{Z} \|Z\|_0 \qquad s.t. \ \|Y - FZ\|_F^2 \leq \varepsilon \tag{13}$$

where $\|\cdot\|_0$ denotes the l_0-norm of matrix Z, $\|\cdot\|_F$ denotes a matrix's Frobenius norm, and ε is a small constant determined by the level of noise. A 2D-CS algorithm (e.g., 2D-SL0, 2D-OMP) can solve the optimization problem posed in (13) [38–40]. However, in practical applications, there is usually a strong noise in the echo. The no sparsity of the noise distribution will seriously affect the reconstruction of the target information, resulting in the loss of important scattering points and false points in the imaging results.

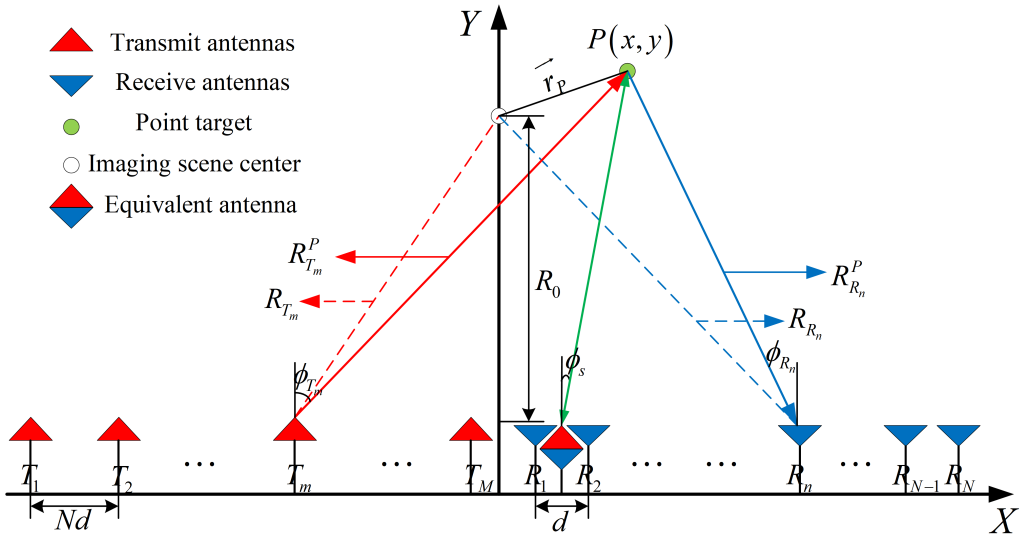


Figure 1. Forward-looking imaging structure model of MIMO radar.

3. Proposed Method

In this section, according to (12), the forward-looking imaging signal model of the MIMO radar combined with sparse and double low-rank constraints is established and then solved by the ALM-ADMM method. First, we analyze the low-rank properties of the signal matrix Y_0 and the image matrix Z.

3.1. Low-Rank Property Analysis

Since the matrix F is a Fourier dictionary matrix, F is a nonsingular matrix. Based on the property of matrix rank, the following equation holds:

$$rank(Y_0) = rank(FZ) = rank(Z) \tag{14}$$

Additionally, the rank of the the signal matrix Y_0 satisfies

$$rank(Y_0) = rank(\sum_{k=1}^{K_0} Y_0^k) \leq \sum_{k=1}^{K_0} rank(Y_0^k) = K_0 \tag{15}$$

where K_0 is the total number of strong scattering point targets in the forward-looking imaging scene.

According to (14) and (15), we have

$$rank(Y_0) = rank(Z) \leq K_0 \tag{16}$$

Equation (16) shows that if the number of strong scattering point targets in the imaging scene is less than the dimension of the echo matrix Y_0, that is, less than MN or Q, then the properties of Y_0 and Z are satisfied simultaneously. Generally, the target we are interested in only accounts for a small part of the whole forward-looking imaging area; i.e., without considering the noise, the energy of the signal matrix Y_0 in the received echo can be represented by several large eigenvalues, which correspond to the information of the strong scattering point targets. Therefore, the signal matrix Y_0 is low-rank, and the resulting image matrix Z is also low-rank. In fact, when the target is sparse, there is an entire zero column or row in the forward-looking image, which can also prove that the image matrix Z is low-rank.

However, when considering the influence of noise, the low-rank characteristics of the echo matrix Y and the image matrix Z are not satisfied. As shown in Figure 2a, the eigenvalue distribution of the signal matrix Y_0, obtained from the point target simulation experiment in Section 4.1, and the echo matrix Y when SNR = 5dB is given. It can be clearly seen that the eigenvalue of the signal matrix Y_0 attenuates rapidly when there is no noise, which indicates the low-rank characteristic of the data. On the contrary, the low-rank property of the echo matrix Y is destroyed due to the high noise energy at a low SNR. Then, the eigenvalue distribution of the image matrix generated by the traditional CS-based imaging method is shown in Figure 2b. It can be seen that the final generated forward-looking image has low-rank characteristics when noise is not considered. However, due to the limited ability of the CS-based imaging method to suppress noise, there are a large number of false targets in the generated image under strong noise conditions, which affects the low-rank characteristics of the image. The above experimental results show that echo signals with low-rank characteristics are crucial for generating high-quality images. Therefore, the image matrix Z and the signal matrix Y_0 can be constrained to a low rank so as to improve their abilities to suppress noise.

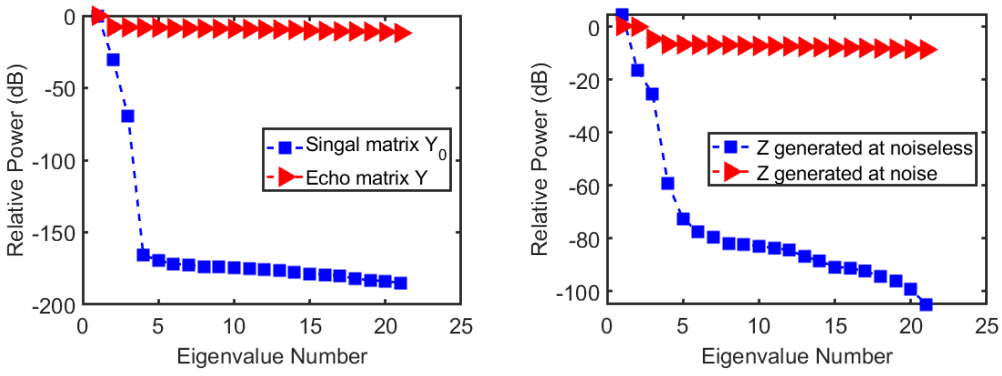


Figure 2. Eigenvalue distribution comparison: (**a**) received echo; (**b**) generated image.

3.2. CSDLR Model and Solution Algorithm

It can be seen from the analysis in Section 3.1 that, in the radar forward-looking imaging, we not only obtain the prior information that the target distribution has sparse characteristics but also realize that the received signal matrix Y_0 and the generated image matrix Z have low-rank properties. Therefore, we can combine the sparsity and double low-rank features to construct a MIMO radar forward-looking image reconstruction model, as shown below.

$$\begin{aligned} \min_{Y_0,Z,E} \ & rank(Y_0) + rank(Z) + \lambda_1 \|Z\|_0 + \lambda_2 \|E\|_F^2 \\ \text{s.t. } & Y_0 = FZ, \\ & Y_0 + E = Y \end{aligned} \tag{17}$$

where $rank(\cdot)$ is the rank function, λ_1 is a regularization parameter used to balance the minimization of the norm and the rank of Z, and λ_2 is a regularization parameter that accounts for the level of noise. The rank function $rank(\cdot)$ and the l_0-norm problems are NP-hard; therefore, we relax $rank(\cdot)$ to the nuclear norm and l_0-norm to the l_1-norm. Then, the optimization problem in (17) can be transformed into the following relaxed convex optimization problem:

$$\begin{aligned} \min_{Y_0,Z,E} \ & \|Y_0\|_* + \|Z\|_* + \lambda_1 \|Z\|_1 + \lambda_2 \|E\|_F^2 \\ \text{s.t. } & Y_0 = FZ, \\ & Y_0 + E = Y \end{aligned} \tag{18}$$

where $\|Y_0\|_* := \sum_i \sigma_i$ and $\|Z\|_* := \sum_j \sigma_j$ denote the nuclear norms of Y_0 and Z, respectively, σ_i is the i-th singular value of Y_0, and σ_j is the j-th singular value of Z.

Obviously, the problem in (18) is a multi-constrained convex problem with separability, so it can be decomposed into several subproblems to be solved separately under the ADMM framework. First, we introduce two auxiliary variables, J_1 and J_2, to make the objective function separable. Then, the convex optimization problem in (18) can be expressed as

$$\begin{aligned} \min_{Y_0,J_1,J_2,E} \ & \|Y_0\|_* + \|J_1\|_* + \lambda_1 \|J_2\|_1 + \lambda_2 \|E\|_F^2 \\ \text{s.t. } & Y_0 - FZ = 0, \\ & Y - FZ - E = 0, \\ & Z - J_1 = 0, Z - J_2 = 0 \end{aligned} \tag{19}$$

The representation for the augmented Lagrange function of (19) is

$$\begin{aligned} L(Y_0, J_1, J_2, Z, E, Q_1, Q_2, Q_3, Q_4) \ = & \|Y_0\|_* + \|J_1\|_* + \lambda_1 \|J_2\|_1 + \lambda_2 \|E\|_F^2 \\ & + Q_1^T (Y_0 - FZ) + \tfrac{u_1}{2} \|Y_0 - FZ\|_F^2 \\ & + Q_2^T (Y - FZ - E) + \tfrac{u_2}{2} \|Y - FZ - E\|_F^2 \\ & + Q_3^T (Z - J_1) + \tfrac{u_3}{2} \|Z - J_1\|_F^2 \\ & + Q_4^T (Z - J_2) + \tfrac{u_4}{2} \|Z - J_2\|_F^2 \end{aligned} \tag{20}$$

where Q_1, Q_2, Q_3, and Q_4 denote the Lagrange multiplier matrices; u_1,u_2,u_3, and u_4 represent the penalty coefficient; and, until a particular convergence condition is reached, the ADMM approach is used to predict the optimal variables Y_0, J_1, J_2, Z, and E, alternately, that is, by estimating one while holding the others constant. The solution to (20) is as follows:

$$\begin{cases} {Y_0}^{k+1} = \arg\min\limits_{Y_0} \left\{ L(Y_0^k, J_1^k, J_2^k, Z^k, E^k, Q_1^k, Q_2^k, Q_3^k, Q_4^k) \right\}, \\ J_1^{k+1} = \arg\min\limits_{J_1} \left\{ L(Y_0^{k+1}, J_1^k, J_2^k, Z^k, E^k, Q_1^k, Q_2^k, Q_3^k, Q_4^k) \right\}, \\ J_2^{k+1} = \arg\min\limits_{J_2} \left\{ L(Y_0^{k+1}, J_1^{k+1}, J_2^k, Z^k, E^k, Q_1^k, Q_2^k, Q_3^k, Q_4^k) \right\}, \\ Z^{k+1} = \arg\min\limits_{z} \left\{ L(Y_0^{k+1}, J_1^{k+1}, J_2^{k+1}, Z^k, E^k, Q_1^k, Q_2^k, Q_3^k, Q_4^k) \right\}, \\ E^{k+1} = \arg\min\limits_{E} \left\{ L(Y_0^{k+1}, J_1^{k+1}, J_2^{k+1}, Z^{k+1}, E^k, Q_1^k, Q_2^k, Q_3^k, Q_4^k) \right\}, \\ Q_1^{k+1} = Q_1^k + \mu_1^k \left(Y_0^{k+1} - FZ^{k+1} \right), \\ Q_2^{k+1} = Q_2^k + \mu_2^k \left(Y - FZ^{k+1} - E^{K+1} \right), \\ Q_3^{k+1} = Q_3^k + \mu_3^k \left(Z^{k+1} - J_1^{k+1} \right), \\ Q_4^{k+1} = Q_4^k + \mu_4^k \left(Z^{k+1} - J_2^{k+1} \right), \\ \mu_1^{k+1} = \rho_1 \mu_1^k, \mu_2^{k+1} = \rho_2 \mu_2^k, \\ \mu_3^{k+1} = \rho_3 \mu_3^k, \mu_4^{k+1} = \rho_4 \mu_4^k. \end{cases} \tag{21}$$

where ρ_1, ρ_2, ρ_3, and ρ_4 are the ratio used to increase u_1,u_2, u_3, and u_4, respectively, and $\rho_1, \rho_2, \rho_3, \rho_4 > 1$.

Updating Y_0

Firstly, the optimization problem of updating Y_0 while fixing J_1, J_2, Z, and E can be expressed as follows:

$$\begin{aligned} Y_0^{k+1} &= \arg\min_{Y_0} \left\| Y_0^k \right\|_* + \left(Q_1^k \right)^T \left(Y_0^k - FZ^k \right) + \tfrac{u_1}{2} \left\| Y_0^k - FZ^k \right\|_F^2 \\ &= \arg\min_{Y_0} \tfrac{1}{Q_1^k} \left\| Y_0^k \right\|_* + \tfrac{1}{2} \left\| Y_0^k - R_1^k \right\|_F^2 \end{aligned} \tag{22}$$

where

$$R_1^k = FZ^k + \frac{Q_1^k}{\mu_1^k} \tag{23}$$

By using the singular value thresholding (SVT) algorithm [41], the nuclear norm minimization problem of (23) was resolved as

$$Y_0^{k+1} = U_1^k soft\left(\Sigma_1^k, \frac{1}{\mu_1^k} \right) \left(V_1^k \right)^H \tag{24}$$

where U_1^k, V_1^k, and Σ_1^k are the singular value decomposition (SVD) results of R_1^k, i.e., $R_1^k = U_1^k \Sigma_1^k \left(V_1^k \right)^H$. Here, U_1^k and V_1^k are unitary matrices, which satisfy $U_1^k \left(U_1^k \right)^H = I$ and $V_1^k \left(V_1^k \right)^H = I$, respectively, and Σ_1^k is all zero except for the elements on the main diagonal. Additionally, $soft(\cdot)$ represents a soft threshold function defined as

$$soft(\Theta, \alpha) = \max\left\{ 1 - \frac{\alpha}{\Theta(i,j)}, 0 \right\} \tag{25}$$

where $\Theta(i,j)$ is a matirx, and α is a constant.

Updating J_1

Secondly, the optimization problem of updating J_1 while fixing Y_0, J_2, Z, and E can expressed as

$$\begin{aligned} J_1^{k+1} &= \arg\min_{J_1} \left\| J_1^k \right\|_* + \left(Q_3^k\right)^T \left(Z^k - J_1^k\right) + \frac{u_3}{2} \left\| Z^k - J_1^k \right\|_F^2 \\ &= \arg\min_{J_1} \frac{1}{Q_3^k} \left\| J_1^k \right\|_* + \frac{1}{2} \left\| J_1^k - R_2^k \right\|_F^2 \end{aligned} \tag{26}$$

where

$$R_2^k = Z^k + \frac{Q_3^k}{\mu_3^k} \tag{27}$$

Similar to the solution process of (22), the nuclear norm minimization problem of (26) can be solved as

$$J_1^{k+1} = U_2^k soft\left(\Sigma_2^k, \frac{1}{\mu_3^k}\right)\left(V_2^k\right)^H \tag{28}$$

where $R_2^k = U_2^k \Sigma_2^k \left(V_2^k\right)^H$.

Updating J_2

Thirdly, the following is the optimization problem of updating J_2, i.e.,

$$\begin{aligned} J_2^{k+1} &= \arg\min_{J_2} \left\| J_2^k \right\|_* + \left(Q_3^k\right)^T \left(Z^k - J_2^k\right) + \frac{u_3}{2} \left\| Z^k - J_2^k \right\|_F^2 \\ &= \arg\min_{J_2} \frac{\lambda_1}{Q_4^k} \left\| J_2^k \right\|_1 + \frac{1}{2} \left\| J_2^k - \left(Z^k + \frac{Q_4^k}{\mu_4^k}\right) \right\|_F^2 \end{aligned} \tag{29}$$

Let $R_3^k = Z^k + \frac{Q_4^k}{\mu_4^k} - \frac{\lambda_1}{Q_4^k}$ and $R_4^k = Z^k + \frac{Q_4^k}{\mu_4^k} + \frac{\lambda_1}{Q_4^k}$. This l_1-norm minimization problem of (29) can be solved as

$$J_2^{k+1} = \max\left(0, R_3^k\right) + \min\left(0, R_4^k\right) \tag{30}$$

Updating Z

Next, the following optimization subproblem of Z needs to be updated as follows

$$\begin{aligned} Z^{k+1} = \arg\min_{Z} & \left(Y_0^{k+1} - FZ^k\right) + \frac{1}{2} \left\| FZ^k - \left(Y_0^{k+1} + \frac{Q_1^k}{\mu_1^k}\right) \right\|_F^2 \\ & + \left(Y - FZ^k - E^k\right) + \frac{1}{2} \left\| FZ^k - \left(Y - E^k + \frac{Q_2^k}{\mu_2^k}\right) \right\|_F^2 \\ & + \left(Z^k - J_1^{k+1}\right) + \frac{1}{2} \left\| Z^k - \left(J_1^{k+1} + \frac{Q_3^k}{\mu_3^k}\right) \right\|_F^2 \\ & + \left(Z^k - J_2^{k+1}\right) + \frac{1}{2} \left\| Z^k - \left(J_2^{k+1} + \frac{Q_4^k}{\mu_4^k}\right) \right\|_F^2 \end{aligned} \tag{31}$$

The minimization optimization issue of (31) can be resolved by the following

$$\begin{aligned} Z^{k+1} = & \left(F^T F + 2I\right) / I \\ & \times \left\{ F^T \left[Y - E^k + Y_0^{k+1} - \left(\frac{Q_1^k}{\mu_1^k} + \frac{Q_2^k}{\mu_2^k} \right) \right] \right. \\ & \left. - \frac{Q_3^k}{\mu_3^k} - \frac{Q_4^k}{\mu_4^k} + J_1^{k+1} + J_1^{k+2} \right\} \end{aligned} \tag{32}$$

Updating E

Lastly, by fixing the others, the update of E can be expressed as

$$\begin{aligned} E^{k+1} &= \arg\min_{E} \lambda_2 \|E\|_F^2 + Q_2^T \left(Y - FZ^{k+1} - E^k\right) \\ &+ \frac{u_2}{2} \left\| Y - FZ^{k+1} - E^k \right\|_F^2 \\ &= \arg\min_{E} \frac{\lambda_2}{Q_2^k} \|E\|_F^2 + \frac{1}{2} \left\| Y - FZ^{k+1} - E^k + \frac{Q_2^k}{\mu_2^k} \right\|_F^2 \end{aligned} \tag{33}$$

The solution to the optimization problem in (33) can be obtained by

$$E^{k+1} = \frac{\mu_2^k\left(Y - FZ^{k+1} + \frac{Q_2^k}{\mu_2^k}\right)}{\lambda_2^k + \mu_2^k} \tag{34}$$

Finally, the whole ALM-ADMM algorithm solution process for the proposed forward-looking imaging model (18) is summarized in Algorithm 1.

Algorithm 1 ALM-ADMM for solving (18)

Input: Measured data matrix $Y \in C^{MN\times Q}$, azimuth dictionary matrix $F \in C^{MN\times\overline{Q}}$, regularization parameter $\lambda_1, \lambda_2 > 0$; iteration number $k = 1$, $Q_1^1 = Q_2^1 = Q_3^1 = Q_4^1 = E^1 = Y_0^1 \in 0^{MN\times Q}$, $J^1 = J^2 = Z^1 \in 0^{U\times Q}$, $u_1^1, u_2^1, u_3^1, u_4^1 > 0$, $\rho_1^1, \rho_2^1, \rho_3^1, \rho_4^1 > 1$.

When the stop condition is not reached, perform
Update Y_0:
$R_1^k = FZ^k + \frac{Q_1^k}{\mu_1^k}$, $R_1^k = U_1^k\Sigma_1^k\left(V_1^k\right)^H$
$Y_0^{k+1} = U_1^k soft\left(\Sigma_1^k, \frac{1}{\mu_1^k}\right)\left(V_1^k\right)^H$
Update J_1:
$R_2^k = Z^k + \frac{Q_3^k}{\mu_3^k}$, $R_2^k = U_2^k\Sigma_2^k\left(V_2^k\right)^H$
$J_1^{k+1} = U_2^k soft\left(\Sigma_2^k, \frac{1}{\mu_3^k}\right)\left(V_2^k\right)^H$
Update J_2:
$R_3^k = Z^k + \frac{Q_4^k}{\mu_4^k} - \frac{\lambda_1}{Q_4^k}$, $R_4^k = Z^k + \frac{Q_4^k}{\mu_4^k} + \frac{\lambda_1}{Q_4^k}$
$J_2^{k+1} = \max\left(0, R_3^k\right) + \min\left(0, R_4^k\right)$
Update Z:
$Z^{k+1} = \left(F^TF + 2I\right)/I \times \left\{F^T\left[Y - E^k + Y_0^{k+1} - \left(\frac{Q_1^k}{\mu_1^k} + \frac{Q_2^k}{\mu_2^k}\right)\right]\right.$
Update E
$E^{k+1} = \frac{\mu_2^k\left(Y - FZ^{k+1} + \frac{Q_2^k}{\mu_2^k}\right)}{\lambda_2^k + \mu_2^k}$
Update $Q_1,\ Q_2,\ Q_3,\ Q_4$:
$Q_1^{k+1} = Q_1^k + \mu_1^k\left(Y_0^{k+1} - FZ^{k+1}\right)$
$Q_2^{k+1} = Q_2^k + \mu_2^k\left(Y - FZ^{k+1} - E^{K+1}\right)$
$Q_3^{k+1} = Q_3^k + \mu_3^k\left(Z^{k+1} - J_1^{k+1}\right)$
$Q_4^{k+1} = Q_4^k + \mu_4^k\left(Z^{k+1} - J_2^{k+1}\right)$
Update $\mu_1,\ \mu_2,\ \mu_3,\ \mu_4$:
$\mu_1^{k+1} = \rho_1\mu_1^k, \mu_2^{k+1} = \rho_2\mu_2^k$
$\mu_3^{k+1} = \rho_3\mu_3^k, \mu_4^{k+1} = \rho_4\mu_4^k$
$k = k + 1$
end while

Output: Z

4. Experiments and Analysis

In this section, we validate the effectiveness of the proposed CSDLR forward-looking imaging method using two simulated experiments and one measured data experiment, in which all experimental results are compared with the conventional MIMO radar BP imaging

method as well as the current CS-based super-resolution imaging methods, including the CS, WCS [33], and JUSLR [30] methods. For all experiments, some parameters are set as follows: $\rho_1 = \rho_2 = \rho_3 = \rho_4 = 1.2$, $u_1^1 = u_2^1 = u_3^1 = u_4^1 = 1.2/\|F\|_F^2$, and the maximum number of iterations is 200. The regularization parameters λ_1 and λ_2 are $[1, 3]$ and $[2, 3]$, respectively.

4.1. Simulated Point Target Results

In this subsection, we use a point target simulation experiment to verify the effectiveness of the proposed CSDLR imaging method. The radar operates in the Ka-band and contains two transmitting antennas and ninety-three receiving antennas. The structure of the radar antenna array is shown in Figure 3, where it can be clearly seen that the MIMO radar equivalent array expands by about double the aperture compared with the actual array. The specific radar operating parameters are shown in Table 1. The radar forward-looking imaging scene contains nine point targets, where the range between two adjacent point targets and the azimuth spacing are 4.1 m, as shown in Figure 4a. According to the radar parameter settings, we can calculate that the range resolution of the MIMO radar in this simulation experiment is about 1 m, and the azimuth resolution is about 16.2 m. Therefore, the traditional MIMO radar BP imaging method cannot distinguish three-point targets within the same range bin, as shown in Figure 4b. Further, the imaging result based on the CS method without noise is given in Figure 4c, and it can be seen that the nine-point targets are clearly distinguishable at this time, which shows the rationality of using CS to achieve super-resolution imaging. Next, Gaussian white noise is added to the radar echoes to generate different SNRs to verify the robustness of the proposed method in a noisy environment.

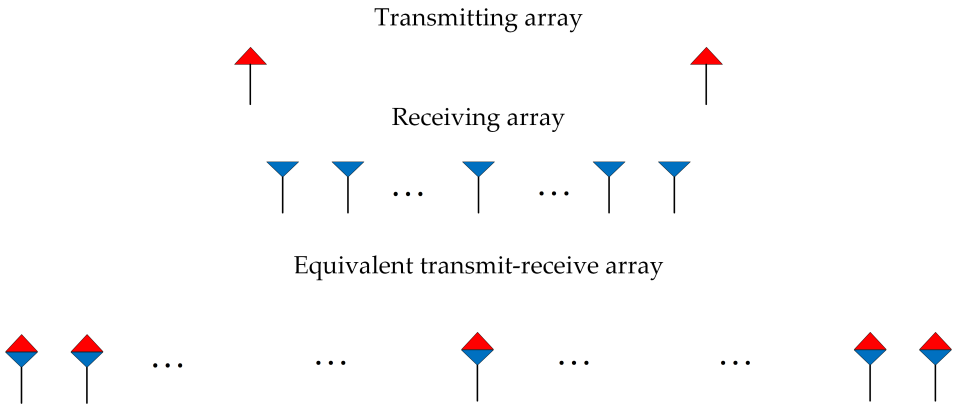


Figure 3. MIMO radar array structure of simulation experiment.

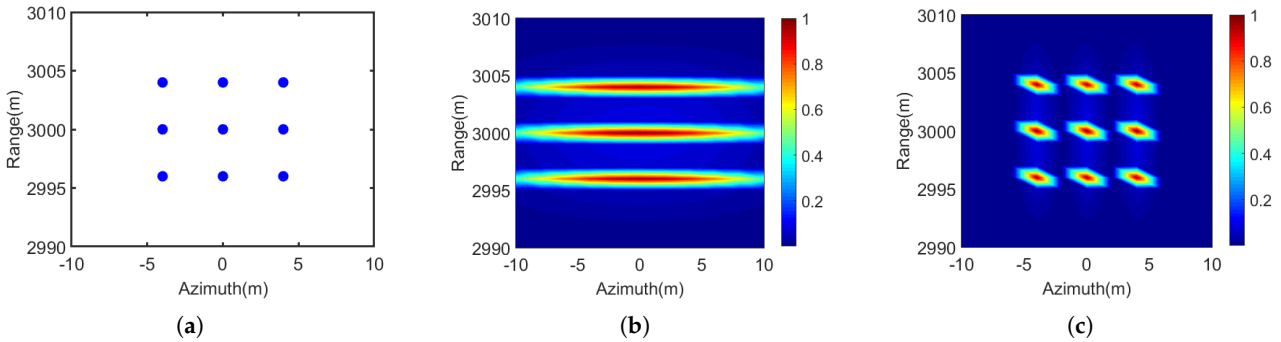


Figure 4. (**a**) Nine-point target distribution: (**b**) BP imaging result; (**c**) CS imaging result.

Table 1. Simulation MIMO radar parameters.

Carrier Frequency	35 GHz	Bandwidth	150 MHz
lambda	8.6 mm	Working distance	3000 m
Transmitting antennas	2	Transmitting antenna spacing	40.0 mm
Receiving antennas	93	Receiving antenna spacing	4.3 mm
Equivalent antennas	186	Equivalent antenna spacing	4.3 mm

First, let us compare the reconstructed forward-looking images of CS, WCS, JUSLR, and the proposed CSDLR method at SNR = 0 dB, 5 dB, and 10 dB. The imaging results are shown in Figure 5, where different rows and columns show the images obtained using different SNRs and different methods, respectively. It can be seen that even at a higher SNR (10 dB), as shown in Figure 5a, the imaging results of the CS and WCS methods are still very poor, and, while the imaging results of the JUSLR method are improved, but it is still difficult to obtain satisfactory forward-looking images in which some targets are not completely distinguished. The proposed CSDLR method has clear and distinguishable nine-point targets. Especially as the SNR decreases, it is obvious from Figure 5b,c that the proposed method can still maintain a better super-resolution imaging capability compared with the other four imaging methods, which confirms the superior performance of the proposed CSDLR imaging method.

Next, we further quantitatively compare the performance of the different imaging methods using two metrics: root mean square error (RMSE) [33] and image correlation (Corr) [29], with a smaller RMSE and a larger Corr indicating a better performance of the imaging method; Figure 4c is used as the reference image. After 200 Monte Carlo experiments, the RMSE and Corr of different imaging methods at SNR = -5 dB, 0 dB, 5 dB, 10 dB, and 15 dB are presented in Figure 6a and Figure 6b, respectively, which clearly show that the RMSE of all methods decreases and the Corr increases as the SNR increases, but the proposed CSDLR method under the same SNR has the lowest RMSE and the largest Corr, especially when the SNR is below 5 dB, which indicates the robustness of the proposed imaging method.

4.2. Simulated Surface Target Results

In the real forward-looking radar imaging scene, the imaging targets are mostly surface targets such as ships, bridges, etc. Therefore, in this section, the performance of the proposed method is verified by using the simulated ship model. We divide the two-dimensional scene of the radar forward-looking imaging into 121 $\times$ 121 grids, in which the distances between the adjacent grids in the range and the azimuth are 1 m and 4 m, respectively. Figure 7a shows the simulated ship model. The ship model is about 105 m long and 17 m wide, including 111 strong scattering points, and all scattering points are located on grid points. The required surface target imaging data are generated using the ship model, in which the radar parameters are the same as in Table 1. When the effect of noise is not considered, the imaging result of the BP-based method for this ship model is given in Figure 7b, where it is obvious that multiple scattering points at the same range bin completely overlap, resulting in blurring of the whole ship. However, the CS-based imaging method can almost perfectly reconstruct the ship in the absence of noise, and the results are shown in Figure 7c, which proves the effectiveness of the CS-based method for super-resolution imaging of the surface target. Then, we verify the imaging performance of the different methods under different SNRs, and Figure 7c is used as the reference image.

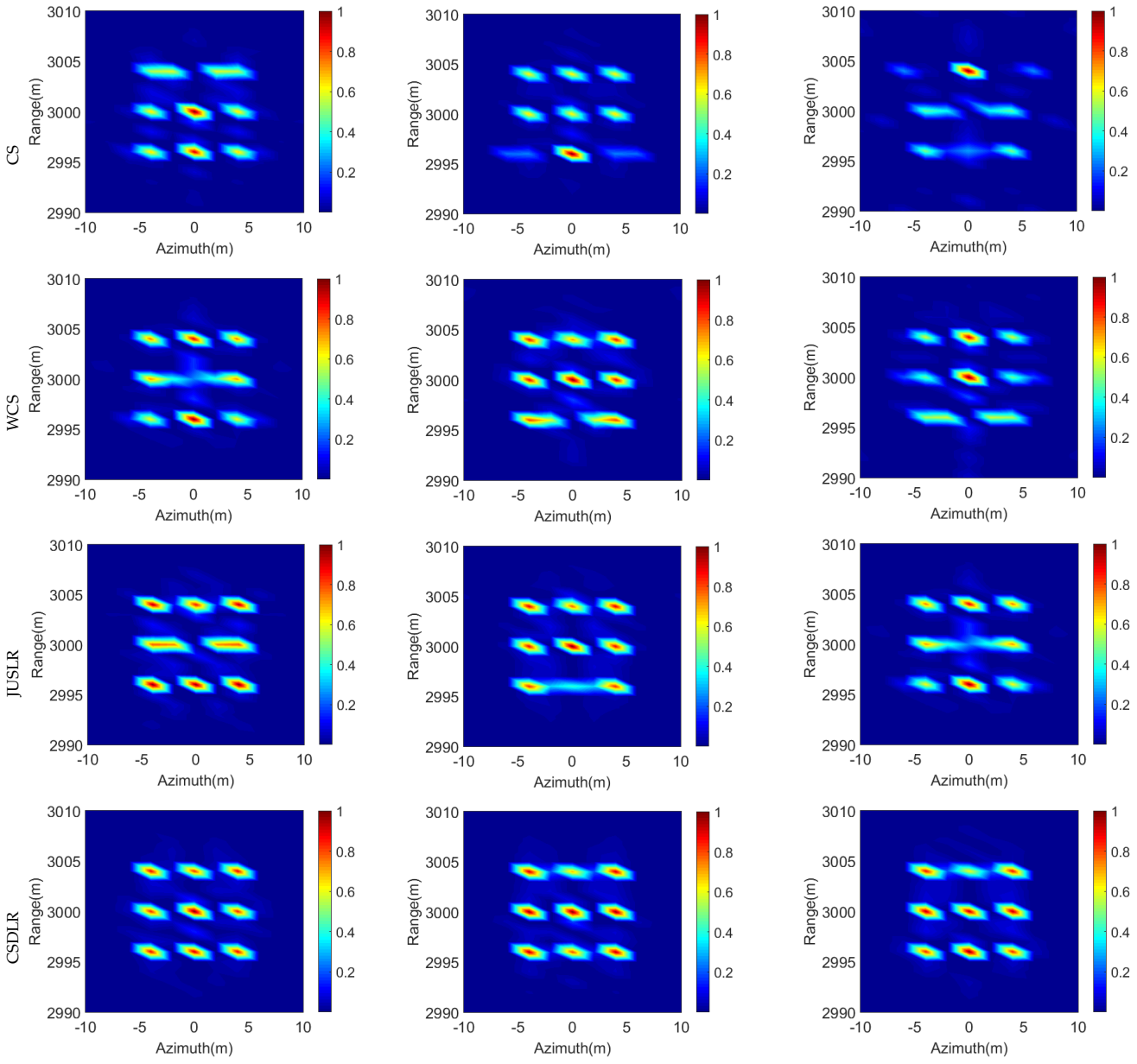


Figure 5. Comparison of imaging results of different methods in nine-point target experiment. (**a**) SNR = 10 dB. (**b**) SNR = 5 dB. (**c**) SNR = 0 dB.

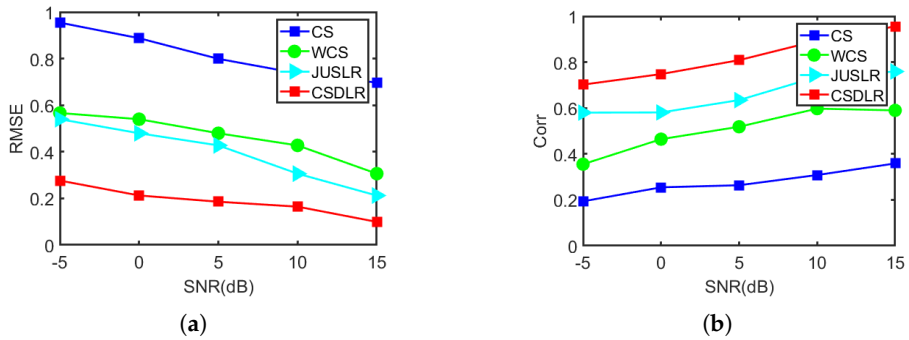


Figure 6. Performance comparison of different imaging methods in point target experiment. (**a**) RMSE. (**b**) Corr.

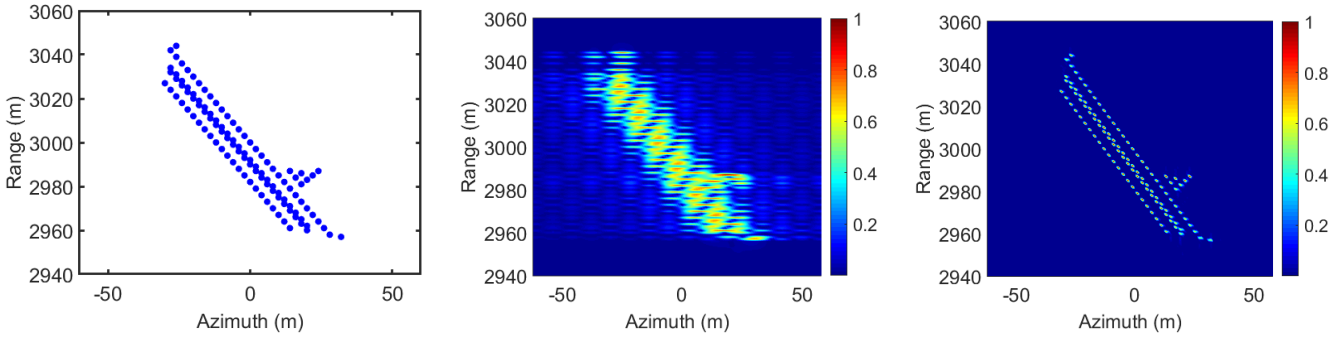


Figure 7. (**a**) Ship target model. (**b**) BP imaging result. (**c**) CS imaging result.

Similar to the point target simulation experiment, for the ship model in Figure 7a, we give four different imaging methods, including CS, WCS, and JULSR, and the imaging results of the proposed CSDLR method under different SNRs, as shown in Figure 8. It can be seen in Figure 8a that, although the ship contour can be seen clearly in the traditional CS method imaging results, the background noise is obvious due to its weak noise suppression ability, and it is difficult to accurately reconstruct the strong scattering points of the ship body. The WCS method improves the ability of noise suppression by changing the noise and target weight, but it is still difficult to obtain satisfactory imaging results. The JUSLR method can eliminate some false point targets by increasing the low-rank constraint prior in the image matrix, but its ability to suppress strong noise is still limited, and, especially with the reduction in the SNR, the imaging performance further deteriorates, as shown in Figure 8b,c. The proposed CSDLR method further enhances the noise suppression ability due to the addition of low-rank constraints on the radar echo. Therefore, even at a low SNR (5 dB), our proposed CSDLR method can still maintain a good imaging performance.

Further, we designed 200 Monte Carlo experiments for different imaging methods to further verify the performance of the proposed imaging methods. Figure 9a,b shows the corresponding RMSE and Corr values of the different SNRs, respectively. According to the curve shown in Figure 9, the proposed CSDLR method has a lower RMSE and Corr, which indicates that the proposed method has an excellent reconstruction performance, especially under low SNR conditions.

4.3. Measured Data Surface Target Results

In this subsection, we use AWR2243 cascaded radar to collect measured data to verify the performance of the proposed CSDLR imaging method. AWR2243 cascade radar is a multi-channel array radar launched by Texas Instruments (TI) that can be applied to long-range radar beam-forming and short-range MIMO radar high-resolution imaging. When AWR2243 cascaded radar works in MIMO mode, the key parameters of the radar are shown in Table 2, including 12 transmitting antennas and 16 receiving antennas, and its equivalent array includes 86 array antennas with half-wavelength spacing, as shown in Figure 10.

Table 2. AWR2243 cascaded radar parameters.

Carrier Frequency	78.7 GHz
Bandwidth	2.5 GHz
lambda	3.8 mm
Transmitting antennas	12
Azimuth transmitting antennas	9
Receiving antennas	16
Azimuth equivalent antennas	86

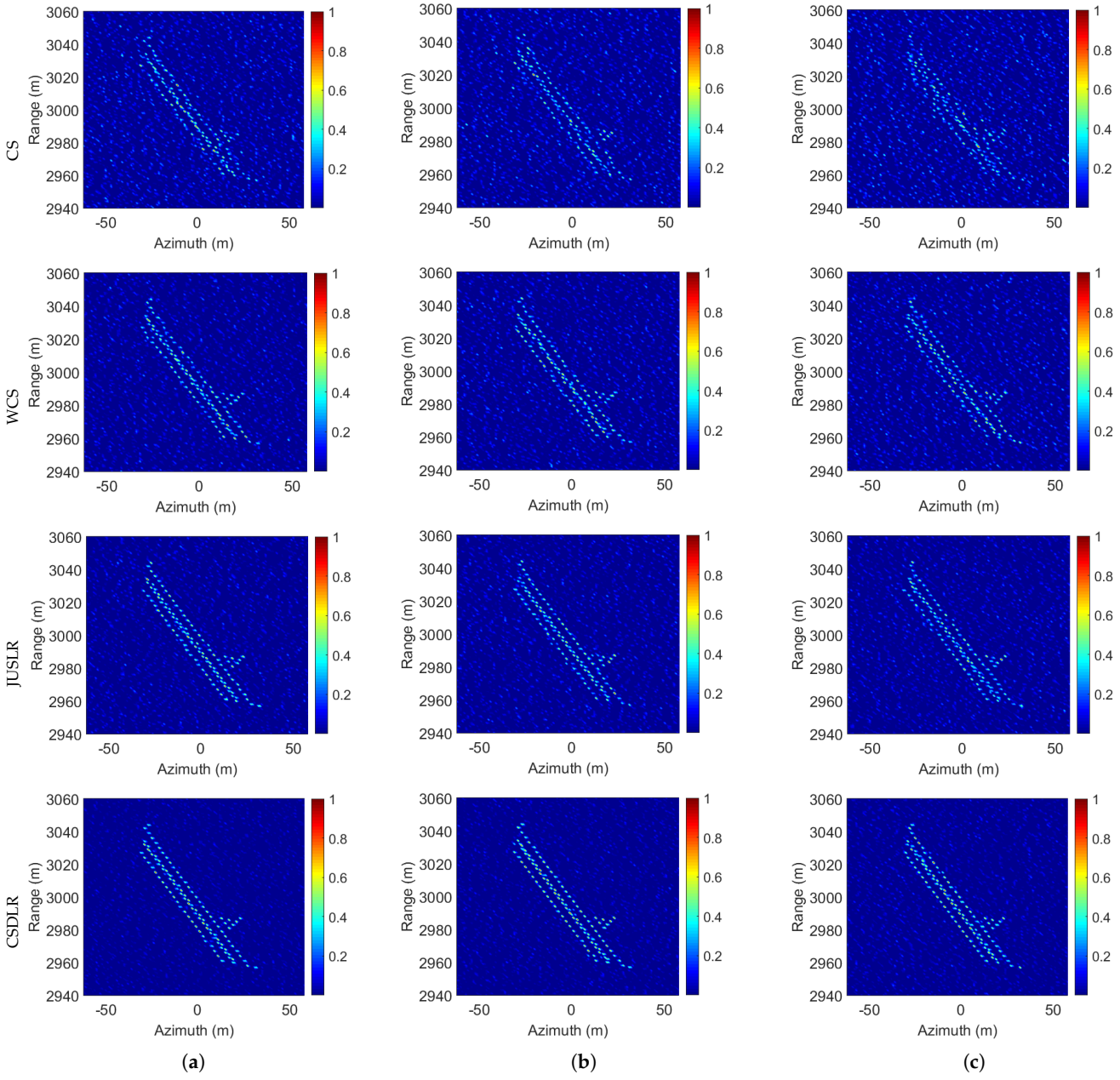


Figure 8. Comparison of imaging results of different methods in ship surface target experiment. (**a**) SNR = 10 dB. (**b**) SNR = 5 dB. (**c**) SNR = 0 dB.

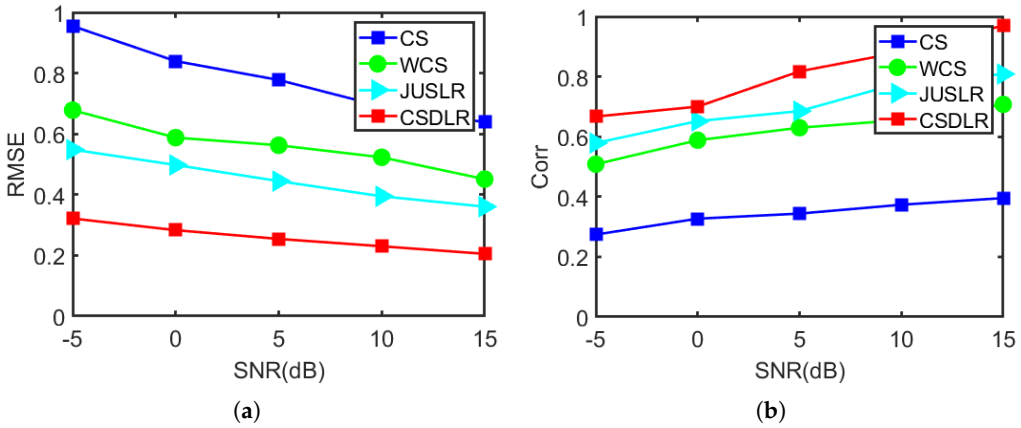


Figure 9. Performance comparison of different imaging methods in ship surface target experiment. (**a**) RMSE. (**b**) Corr.

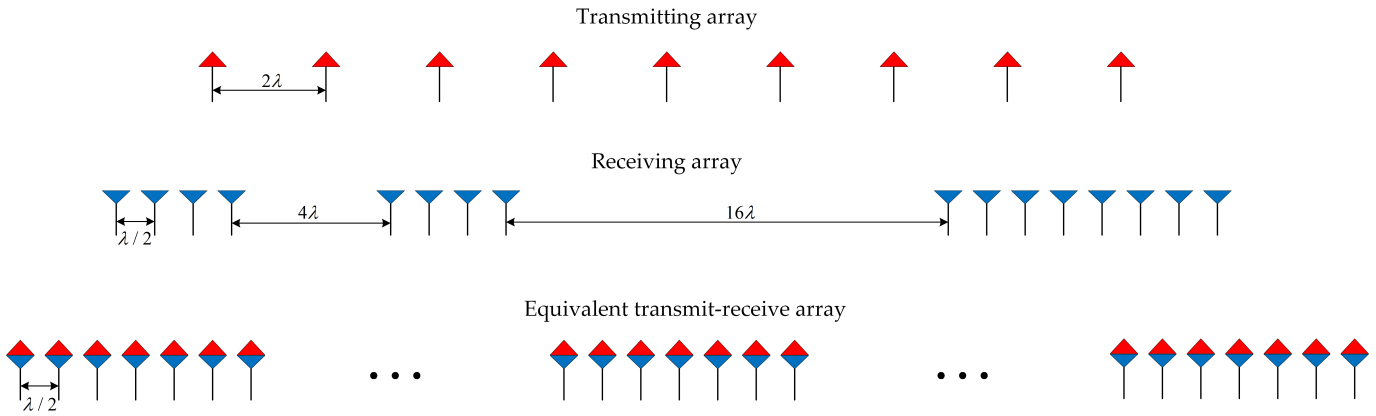
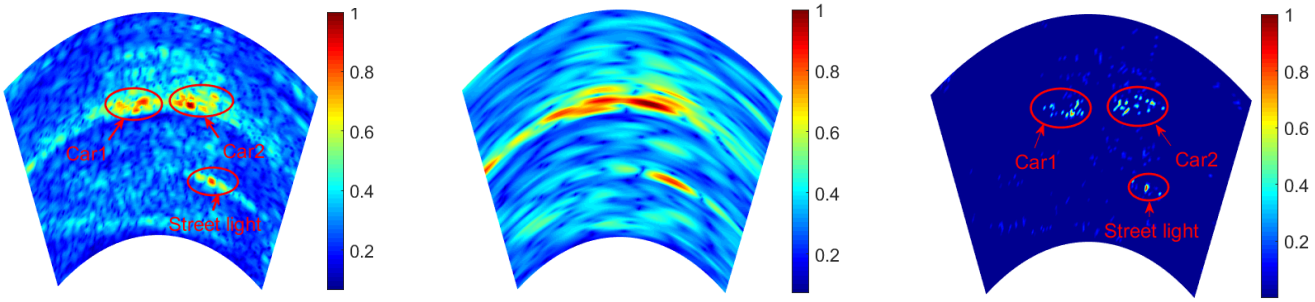


Figure 10. Array structure of AWR2243 cascaded radar.

The experimental site was chosen in a parking lot of Xidian University, China, where the experimental scenario contains two cars and a street light, and we fixed the radar equipment on a tripod to collect the data, as shown in Figure 11. Figure 12a gives the imaging results of all 86 equivalent antenna echoes based on the BP method, which shows that the two cars are clearly distinguishable, and the street light is obvious. The imaging results of using the equivalent array, of which 124 antennas echo data, also using the BP imaging method, are shown in Figure 12b. At this time, the two cars overlap one another, and the street lights are diffused seriously. Therefore, we can use these 24 antenna echoes to verify the proposed super-resolution imaging method. In addition, in Figure 12c, we present the imaging results of the 86-antenna echo data based on the CS method, and it can be clearly seen that the CS imaging method has the advantages of low side flap and high resolution compared with the BP imaging method, which justifies the proposal of a CS-based method to improve the resolution of the forward-looking imaging in this paper. Since the SNR of the raw radar echo data is high (about 18 dB), we add Gaussian white noise to the radar echoes to generate different SNRs to verify the noise robustness of the proposed CSDLR imaging method, and Figure 12c is used as the reference image.



Figure 11. Experimental scenario.



(**a**) (**b**) (**c**)

Figure 12. (**a**) BP imaging result of 86 full-aperture antenna echoes. (**b**) BP imaging result of 24 partial-aperture antenna echoes. (**c**) CS imaging result of 86 full-aperture antenna echoes.

Figure 13 depicts the imaging results of the four different methods at three different SNR levels. We can clearly see that, under the same SNR, the images generated by the traditional CS method and the WCS method make it difficult to distinguish between the two vehicles, and a large number of false targets appear. Although the JUSLR method can roughly distinguish between the two cars, there are still false targets at the street lamps and other locations. The proposed CSDLR method can produce satisfactory imaging results: the two cars can be clearly distinguished, and the false targets at the location of street lamps are basically suppressed. Subsequently, the Corr and RMSE of the different methods are calculated, and the results are shown in Table 3. From the table, we can clearly see that the CSDLR method proposed by us has the highest Corr value and the lowest RMSE value under the same SNR, especially in a strong noise environment, which proves the superior performance of our method.

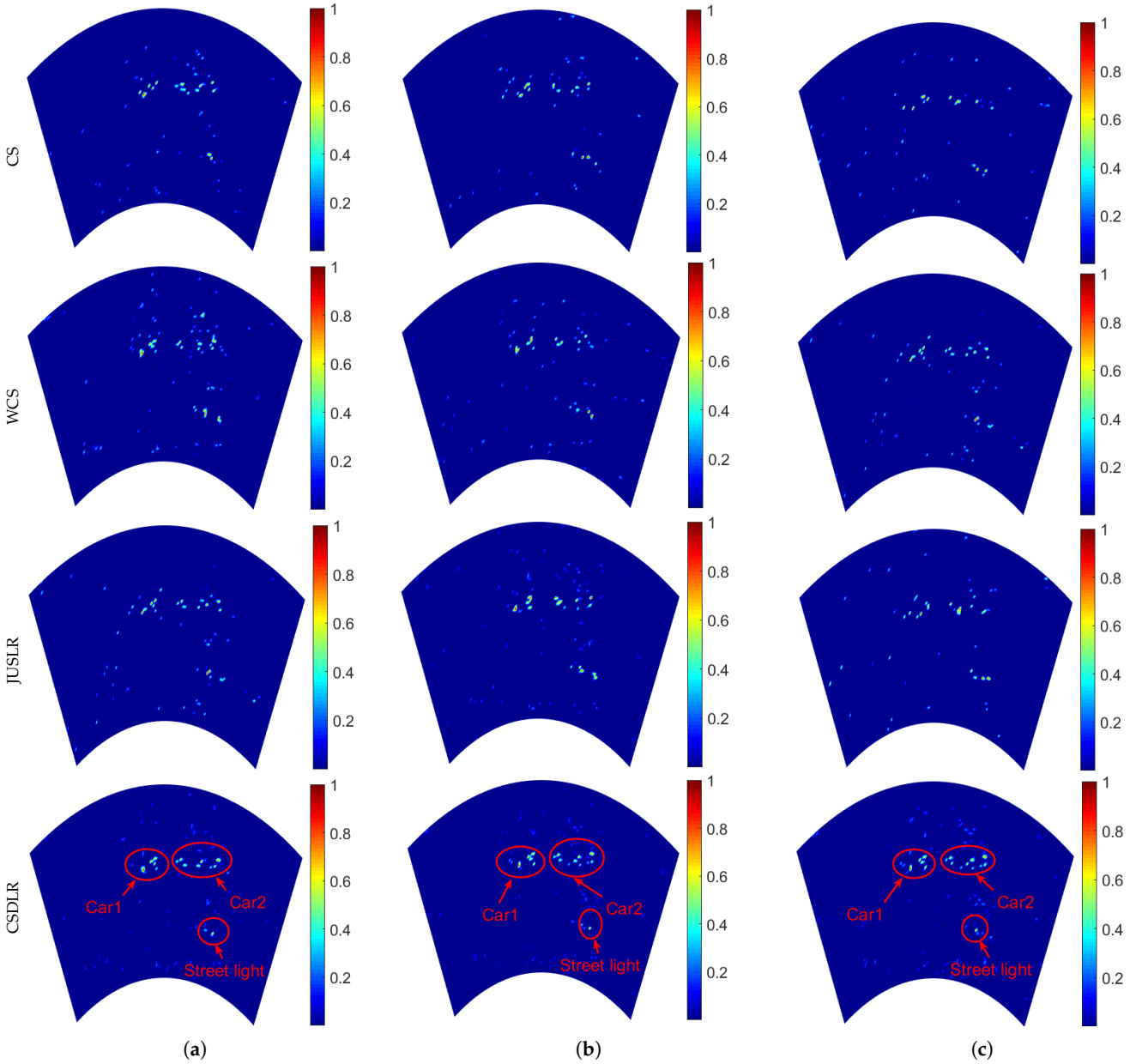


Figure 13. Comparison of imaging results of different methods in measured data experiment. (**a**) SNR = 10 dB. (**b**) SNR = 5 dB. (**c**) SNR = 0 dB.

Table 3. Comparison of RMSE and Corr of different imaging methods in measured data experiment.

Method	RMSE			Corr		
	10 dB	5 dB	0 dB	10 dB	5 dB	0 dB
CS	0.65	0.82	0.92	0.36	0.22	0.18
WCS	0.60	0.75	0.80	0.52	0.48	0.46
JUSLR	0.45	0.53	0.62	0.60	0.58	0.55
CSDLR	0.15	0.20	0.24	0.93	0.90	0.86

Finally, we evaluate the computational efficiency by comparing the running times of the different imaging methods. All methods in the measured data processing are coded by Matlab 2018b and run on a personal computer, where the computer is configured as follows: CPU is i7-7800@3.2 GHz, 16 GB RAM. The average time of 100 Monte Carlo experiments

for the different imaging methods is shown in Table 4. It can be seen from Table 4 that the BP method has the highest efficiency (1.75 s) in imaging, where the data matrix is 256×86. The CS method and the WCS method have almost the same working speed, but, due to the large dictionary matrix involved and the high computational complexity of each step, the operation time is long. The ADMM is very suitable for large-scale computing because it combines the advantages of the strong convergence of the multiplier method with the decomposability of the dual rise method. Therefore, the running speeds of the JUSLR and CSDLR methods are higher than those of the CS and WCS methods. In addition, the proposed CSDLR method has more constraints than the JUSLR method, so the imaging time is longer.

Table 4. Comparison of running time of different imaging methods in measured data experiment.

Method	BP	CS	WCS	JUSLR	CSDLR
Running time (s)	1.75	7.40	7.56	3.01	3.78

5. Conclusions

This paper presents an effective method for enhancing the forward-looking imaging resolution of radar under a limited aperture. In addition to the sparsity of the targets commonly used in traditional CS-based imaging methods, the inherent relationship between the echo signal and the characteristics of forward-looking radar images is used to improve the image quality. Specifically, a forward-looking super-resolution imaging method combining the sparse and dual low-rank features of the MIMO radar is proposed. One of the low-rank features refers to the energy of the echo signal, which can be represented by several large eigenvalues when noise is not considered, i.e., the echo signal has a low-rank feature; another low rank refers to the inherent characteristics of forward-looking radar images. In addition, an ALM-ADMM-based algorithm is proposed to effectively solve the proposed multiple optimization constraint problem model. Finally, the experiments using the simulation and measurement data show that our algorithm is not only capable of forward-looking super-resolution imaging but is also noise robust. When the SNR is over 0dB, the CSDLR imaging method that we propose can produce at least four times the super-resolution imaging in simulation experiments and at least three and a half times the super-resolution imaging in measured data experiments compared to the BP imaging method.

It should be pointed out that the method proposed in this paper only suppresses the noise in radar imaging, but there is a lot of clutter in the actual scene. If the clutter is not suppressed, the subsequent target detection will be affected. Therefore, noise and clutter suppression will be considered in future research so that the proposed method can be applied to more scenes.

Author Contributions: J.T. conceived the main idea, designed the experiments, wrote the MATLAB code, and wrote the manuscript. Z.L. reviewed the manuscript. L.R. sourced the funding and reviewed the manuscript. R.X. sourced the funding. J.Q. checked the spelling of the paper. All authors have read and agreed to the published version of the manuscript.

Funding: This work was funded in part by the National Natural Science Foundation of China under Grant 62001346 and the China Postdoctoral Science Foundation under Grant 2019M663632. It was also funded by the Science and Technology on Plasma Dynamics Laboratory, Air Force Engineering University, No. 6142202210305, and the Seed Funding Project of Multisensor Intelligent Detection and Recognition Technologies R&D Center of CASC, No. ZZJJ202102.

Acknowledgments: The authors would like to thank the anonymous reviewers for their constructive comments to improve the quality of this paper.

Institutional Review Board Statement: Not applicable.

Informed Consent Statement: Not applicable.

Data Availability Statement: Not applicable.

Conflicts of Interest: The authors declare no conflict of interest.

References

1. Mao, D.; Zhang, Y.; Pei, J.; Huo, W.; Zhang, Y.; Huang, Y.; Yang, J. Forward-looking geometric configuration optimization design for spaceborne-airborne multistatic synthetic aperture radar. *IEEE J. Sel. Top. Appl. Earth Obs. Remote Sens.* **2021**, *14*, 8033–8047. [CrossRef]
2. Kim, S.; Ka, M.H. Forward-looking electromagnetic wave imaging using a radial scanning multichannel radar. *IEEE Geosci. Remote Sens. Lett.* **2021**, *19*, 1–5. [CrossRef]
3. Huang, Y.; Zha, Y.; Wang, Y.; Yang, J. Forward looking radar imaging by truncated singular value decomposition and its application for adverse weather aircraft landing. *Sensors* **2015**, *15*, 14397–14414. [CrossRef]
4. Li, W.; Li, M.; Zuo, L.; Sun, H.; Chen, H.; Li, Y. Forward-Looking Super-Resolution Imaging for Sea-Surface Target with Multi-Prior Bayesian Method. *Remote Sens.* **2021**, *14*, 26. [CrossRef]
5. Ran, L.; Liu, Z.; Xie, R. Ground Maneuvering Target Focusing via High-Order Phase Correction in High-Squint Synthetic Aperture Radar. *Remote Sens.* **2022**, *14*, 1514. [CrossRef]
6. Ran, L.; Liu, Z.; Xie, R.; Zhang, L. Focusing high-squint synthetic aperture radar data based on factorized back-projection and precise spectrum fusion. *Remote Sens.* **2019**, *11*, 2885. [CrossRef]
7. Zheng, J.; Chen, R.; Yang, T.; Liu, X.; Liu, H.; Su, T.; Wan, L. An efficient strategy for accurate detection and localization of UAV swarms. *IEEE Internet Things J.* **2021**, *8*, 15372–15381. [CrossRef]
8. Chen, S.; Yuan, Y.; Zhang, S.; Zhao, H.; Chen, Y. A new imaging algorithm for forward-looking missile-borne bistatic SAR. *IEEE J. Sel. Top. Appl. Earth Obs. Remote Sens.* **2016**, *9*, 1543–1552. [CrossRef]
9. Duan, G.Q.; Wang, D.W.; Ma, X.Y.; Su, Y. Three-dimensional imaging via wideband MIMO radar system. *IEEE Geosci. Remote Sens. Lett.* **2010**, *7*, 445–449. [CrossRef]
10. Bekkerman, I.; Tabrikian, J. Target detection and localization using MIMO radars and sonars. *IEEE Trans. Signal Process.* **2006**, *54*, 3873–3883. [CrossRef]
11. Schindler, D.; Schweizer, B.; Knill, C.; Hasch, J.; Waldschmidt, C. Synthetization of virtual transmit antennas for MIMO OFDM radar by space-time coding. *IEEE Trans. Aerosp. Electron. Syst.* **2020**, *57*, 1964–1971. [CrossRef]
12. Chen, H.; Li, X.; Jiang, W.; Zhuang, Z. MIMO radar sensitivity analysis of antenna position for direction finding. *IEEE Trans. Signal Process.* **2012**, *60*, 5201–5216. [CrossRef]
13. Zhang, F.; Sun, G.; Zhou, Y.; Gao, B.; Pan, S. Towards High-Resolution Imaging With Photonics-Based Time Division Multiplexing MIMO Radar. *IEEE J. Sel. Top. Quantum Electron.* **2022**, *28*, 1–10. [CrossRef]
14. Song, Y.; Hu, J.; Chu, N.; Jin, T.; Zhang, J.; Zhou, Z. Building layout reconstruction in concealed human target sensing via UWB MIMO through-wall imaging radar. *IEEE Geosci. Remote Sens. Lett.* **2018**, *15*, 1199–1203. [CrossRef]
15. Zhou, L.; Su, Y. GPR imaging with RM algorithm in layered mediums. *IEEE Geosci. Remote Sens. Lett.* **2011**, *8*, 934–938. [CrossRef]
16. Li, X.; Kong, L.; Cui, G.; Yi, W.; Yang, Y. ISAR imaging of maneuvering target with complex motions based on ACCF–LVD. *Digital Signal Process.* **2015**, *46*, 191–200. [CrossRef]
17. Wu, K.; Cui, W.; Xu, X. Superresolution Radar Imaging via Peak Search and Compressed Sensing. *IEEE Geosci. Remote Sens. Lett.* **2022**, *19*, 1–5. [CrossRef]
18. Pan, X.Y.; Wang, W.; Wang, G.Y. Sub-Nyquist sampling jamming against ISAR with CS-based HRRP reconstruction. *IEEE Sens. J.* **2015**, *16*, 1597–1602. [CrossRef]
19. He, C.; Zhuo, T.; Ou, D.; Liu, M.; Liao, M. Nonlinear compressed sensing-based LDA topic model for polarimetric SAR image classification. *IEEE J. Sel. Top. Appl. Earth Obs. Remote Sens.* **2013**, *7*, 972–982. [CrossRef]
20. Yang, J.; Jin, T.; Xiao, C.; Huang, X. Compressed sensing radar imaging: Fundamentals, challenges, and advances. *Sensors* **2019**, *19*, 3100. [CrossRef]
21. Zhang, W.; Hoorfar, A. A generalized approach for SAR and MIMO radar imaging of building interior targets with compressive sensing. *IEEE Antennas Wirel. Propag. Lett.* **2015**, *14*, 1052–1055. [CrossRef]
22. Li, H.; Li, S.; Li, Z.; Dai, Y.; Jin, T. Compressed sensing imaging with compensation of motion errors for MIMO Radar. *Remote Sens.* **2021**, *13*, 4909. [CrossRef]
23. Wang, Y.; Li, X. 3-D imaging based on combination of the ISAR technique and a MIMO radar system. *IEEE Trans. Geosci. Remote Sens.* **2018**, *56*, 6033–6054. [CrossRef]
24. Feng, W.; Friedt, J.M.; Nico, G.; Sato, M. 3-D ground-based imaging radar based on C-band cross-MIMO array and tensor compressive sensing. *IEEE Geosci. Remote Sens. Lett.* **2019**, *16*, 1585–1589. [CrossRef]
25. Hu, X.; Tong, N.; Zhang, Y.; Huang, D. MIMO radar imaging with nonorthogonal waveforms based on joint-block sparse recovery. *IEEE Trans. Geosci. Remote Sens.* **2018**, *56*, 5985–5996. [CrossRef]
26. Miller, M.; Hinze, J.; Saquib, M.; Blanchard, A.J. Adjustable transmitter spacing for MIMO radar imaging with compressed sensing. *IEEE Sens. J.* **2015**, *15*, 6671–6677. [CrossRef]
27. Gu, F.; Chi, L.; Zhang, Q.; Zhu, F. Single snapshot imaging method in multiple-input multiple-output radar with sparse antenna array. *IET Radar Sonar Navig.* **2013**, *7*, 535–543. [CrossRef]
28. Ding, J.; Wang, M.; Kang, H.; Wang, Z. MIMO radar super-resolution imaging based on reconstruction of the measurement matrix of compressed sensing. *IEEE Geosci. Remote Sens. Lett.* **2021**, *19*, 1–5. [CrossRef]

29. Qiu, W.; Zhou, J.; Fu, Q. Jointly using low-rank and sparsity priors for sparse inverse synthetic aperture radar imaging. *IEEE Trans. Image Process.* **2019**, *29*, 100–115. [CrossRef] [PubMed]
30. Lv, M.J.; Chen, W.F.; Ma, J.c.; Cheng, Q.; Yang, J.; Ma, X.Y. Enhanced sparse ISAR imaging by jointly using sparsity and low-rank properties. *Digital Signal Process.* **2021**, *118*, 103242. [CrossRef]
31. Zhang, X.; Bai, T.; Meng, H.; Chen, J. Compressive sensing-based ISAR imaging via the combination of the sparsity and nonlocal total variation. *IEEE Geosci. Remote Sens. Lett.* **2013**, *11*, 990–994. [CrossRef]
32. Zeng, C.; Zhu, W.; Jia, X.; Yang, L. Sparse aperture ISAR imaging method based on joint constraints of sparsity and low rank. *IEEE Trans. Geosci. Remote Sens.* **2020**, *59*, 168–181. [CrossRef]
33. Zhang, L.; Xing, M.; Qiu, C.W.; Li, J.; Sheng, J.; Li, Y.; Bao, Z. Resolution enhancement for inversed synthetic aperture radar imaging under low SNR via improved compressive sensing. *IEEE Trans. Geosci. Remote Sens.* **2010**, *48*, 3824–3838. [CrossRef]
34. Lu, C.; Feng, J.; Yan, S.; Lin, Z. A unified alternating direction method of multipliers by majorization minimization. *IEEE Trans. Pattern Anal. Mach. Intell.* **2017**, *40*, 527–541. [CrossRef]
35. Lu, X.; Lü, X. ADMM for image restoration based on nonlocal simultaneous sparse Bayesian coding. *Signal Process. Image Commun.* **2019**, *70*, 157–173. [CrossRef]
36. Johnston, J.; Li, Y.; Lops, M.; Wang, X. ADMM-net for communication interference removal in stepped-frequency radar. *IEEE Trans. Signal Process.* **2021**, *69*, 2818–2832. [CrossRef]
37. Kwan, C.; Choi, J.H.; Chan, S.H.; Zhou, J.; Budavari, B. A super-resolution and fusion approach to enhancing hyperspectral images. *Remote Sens.* **2018**, *10*, 1416. [CrossRef]
38. Feng, W.; Zhang, Y.; Guo, Y.; He, X. 2D OMP algorithm for space–time parameters estimation of moving targets. *Electron. Lett.* **2015**, *51*, 1809–1811. [CrossRef]
39. Yin, Z.; Lu, X.; Chen, W. Echo preprocessing to enhance SNR for 2D CS-based ISAR imaging method. *Sensors* **2018**, *18*, 4409. [CrossRef]
40. Hashempour, H.R. Sparsity-driven ISAR imaging based on two-dimensional ADMM. *IEEE Sens. J.* **2020**, *20*, 13349–13356. [CrossRef]
41. Cai, J.F.; Candès, E.J.; Shen, Z. A singular value thresholding algorithm for matrix completion. *SIAM J. Optim.* **2010**, *20*, 1956–1982. [CrossRef]

Disclaimer/Publisher's Note: The statements, opinions and data contained in all publications are solely those of the individual author(s) and contributor(s) and not of MDPI and/or the editor(s). MDPI and/or the editor(s) disclaim responsibility for any injury to people or property resulting from any ideas, methods, instructions or products referred to in the content.